Enhanced Modulation Strategy and Magnetic Component Parameter Design for Dual Active Bridge Converters to Improve Efficiency Under Variable Load Conditions

Hongwei Zhang, *Student Member, IEEE*, and Zeng Liu, *Senior Member, IEEE*

***Abstract*—Dual active bridge converter serves as the hub for energy exchange, with efficiency being its paramount indicator. A comprehensive optimization solution for efficiency improvement is proposed in this article, which consists of two parts. The part one is an optimal modulation strategy that achieves full soft switching under light-load conditions, minimizes peak current under heavy-load conditions, and enables seamless transitions between different modes. The part two is the optimization of magnetic component parameters, specifically the turns ratio and inductance, based on this modulation strategy to further reduce the current stress and enhance overall efficiency. Distinct from the previous work, the proposed solution offers noteworthy advantages: 1) the modulation strategy attains zero-voltage switching (ZVS) instead of quasi-ZVS under light-load conditions and facilitates seamless mode transitions; 2) the turns ratio and inductance are tailored for variable load conditions, rendering them applicable to a more extensive array of scenarios; 3) the analytical design method for magnetic component parameters enhances both the portability and accuracy compared to traditional exhaustive search methods. The experimental results confirm the theoretical analysis and illustrate the effectiveness and superiority of the proposed solution.**

***Index Terms*—Current stress, dual active bridge (DAB), magnetic component parameters, soft switching, variable load condition.**

I. Introduction

AMIDST the rapid expansion of renewable energy sources, isolated bidirectional dc–dc converters have witnessed widespread deployment. The dual active bridge (DAB) converter [1], distinguished by its galvanic isolation, soft-switching capability, and bidirectional power flow capability, has found universal application across diverse domains, including distributed generation, electric vehicles, and smart grids [2], [3], [4], [5], [6].

As the central hub for energy interaction, the efficiency of DAB converters is of paramount significance. Existing research aimed at enhancing the efficiency of DAB converters can be broadly categorized into two primary methods. The first is to establish the total loss model [7], [8], [9], and then optimize the factors of such models to enhance the efficiency. The total loss of DAB converters primarily comprises the switching loss, ohmic loss, and core loss. The switching loss is mainly affected by the peak current and the junction capacitors of the switching devices, while the ohmic loss is primarily affected by the rms current, winding resistance, and ON-resistance of switching devices. Additionally, the core loss chiefly depends on the peak current, core volume, and core material. It should be noted that the parasitic parameters of the devices, specifically the ac resistance and magnetic flux density, are influenced by specific operating conditions and environment. Hence, establishing a precise total loss model is frequently challenging, and the utility of such models is generally constrained. The second method entails quantifying the total loss by examining the waveform of inductor current, thereby simplifying the total loss model. Early research utilized backflow power as an indicator to evaluate the losses [10], [11], leading to elevated ohmic losses. Subsequent research has revealed that the rms current [12], [13], unlike the backflow power, has a more direct impact on ohmic losses. Since switching losses account for a substantial portion of total losses, many studies have integrated rms current optimization with the implementation of soft switching techniques [14], [15] to further enhance the efficiency. Similarly, the peak current optimization can be combined with soft switching [16], [17], [18], [19]. Given the close relationship between the peak current and switching losses, reducing peak current can not only decrease core losses but also mitigate switching losses. Hence, this article utilizes the minimization of peak current with soft switching as a metric for enhancing the efficiency.

The reduction of peak current and the expansion of the soft-switching range can be categorized into two main approaches: one involves optimization through modulation strategies, while the other focuses on optimization through magnetic component parameters.

Received 7 October 2024; revised 24 January 2025; accepted 24 February 2025. Date of publication 7 April 2025; date of current version 26 May 2025. This work was supported by the National Key Research and Development Program of China under Grant 2023YFB2604600. Recommended for publication by Associate Editor M. Su. *(Corresponding author: Zeng Liu.)*

The authors are with the State Key Laboratory of Electrical Insulation and Power Equipment, School of Electrical Engineering, Xi'an Jiaotong University, Xi'an 710049, China (e-mail: zhw0625@stu.xjtu.edu.cn; zengliu@mail.xjtu.edu.cn).

Color versions of one or more figures in this article are available at https://doi.org/10.1109/TPEL.2025.3558396.

Digital Object Identifier 10.1109/TPEL.2025.3558396

The predominant methods of existing research for the peak current reduction involve the modulation strategy optimization. The DAB converter has 4 legs, allowing for up to 3 phase-shift ratios. The control method that employs only one phase-shift ratio is referred to as single-phase-shift (SPS) control. Due to its limited degree of freedom, SPS control is confined to regulating the transmission power but cannot contribute to the optimization of peak current. Double-phase-shift control [20], [21] and extended-phase-shift control [22], [23] both utilize two phase-shift ratios, enabling achieving the soft switching and peak current reduction while controlling the transmission power. In [16], [17], and [18], all available degrees of freedom are effectively employed, and a method for achieving the minimum peak current under triple-phase-shift (TPS) control is proposed. However, this method leads to six devices achieving quasi-zero-voltage switching (QZVS) under light-load conditions, consequently reducing efficiency. In [24], a modulation strategy that ensures all switching devices achieve zero-voltage switching (ZVS) under light-load conditions while minimizing the peak current under heavy-load conditions is proposed. However, the phase-shift ratios show discontinuities across the entire power range. The primary aim of optimizing the modulation strategy is to modify the waveform of the inductor voltage. However, these methods overlook the impact of inductance and turns ratio on the inductor current, thus hindering the attainment of the minimum peak current. Given that the modulation strategy optimization serves as the basis for the magnetic component optimization [25], this article will devise an optimal modulation strategy that achieves full ZVS under light-load modes, minimizes the peak current under heavy-load modes, and facilitates seamless transitions between different modes.

To overcome the limitations of exclusively focusing on the modulation strategy optimization, the optimization methods for magnetic component parameters are introduced. It is crucial to emphasize that modulation strategy optimization and magnetic component parameter optimization are independent processes, permitting the design of magnetic component parameters based on various modulation strategies. There is a scarcity of research focused on the magnetic component parameter optimization, with the majority of studies primarily based on SPS control [26], [27], [28], [29], [30]. In [26], [27], and [28], soft switching can be achieved under light-load conditions through the optimization of inductance, turns ratio, and excitation inductance, respectively. In [29], an empirical algorithm for the turns ratio and inductance is proposed, which maintains the voltage ratio of 1 under rated conditions. However, this method overlooks the optimization for other operating points. In [30], an exhaustive search method is used to design the optimal turns ratio and inductance for wide output voltage conditions aimed at minimizing the current stress or rms current. However, this method cannot obtain theoretical solutions, and its accuracy depends on the search step. Worse still, when the optimal magnetic component parameters lie outside the search range, the designed parameters may cause a significant increase in peak current. In summary, the parameter design method based on SPS control has limited degrees of freedom, making it challenging to optimize both peak current and soft switching simultaneously.

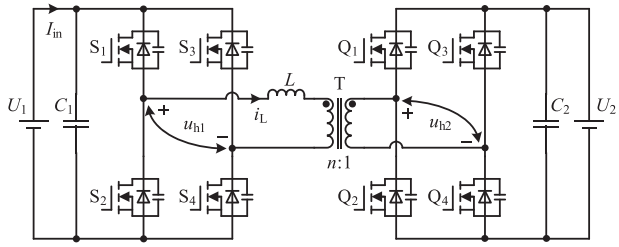

Fig. 1. Diagram of DAB converter.

The design methods for magnetic component parameters based on TPS control are proposed [25], [31], providing additional degrees of freedom. In [31], the design method for rms current reduction with soft switching implementation is proposed, which can potentially enhance the efficiency. However, the voltage ratios designed in this method are consistently smaller than 1, limiting the optimization of both rms current and current stress to a significant extent. In [25], the current stress can be minimized by judiciously configuring the voltage ratio and per-unit power. However, this method is tailored to constant output current conditions, limiting its applicability to a narrow range of operating conditions. If this method is employed for variable load conditions, most operating points would operate under light-load conditions, leading to the loss of soft switching and reduced efficiency.

In this article, a novel design methodology for efficiency improvement is introduced. This method can not only further enhance the efficiency by achieving soft switching under light-load conditions but also extend its applicability to a broader range of operating conditions. The main contributions are outlined as follows. First, the factors influencing the peak current and soft switching under variable load conditions are comprehensively analyzed. Second, an optimal modulation strategy is derived, considering the impact of the junction capacitors of switching devices on soft switching. This strategy seeks to minimize peak current and achieve ZVS under light-load conditions, while ensuring seamless transitions between different modes. Third, the impact of per-unit power and voltage ratio on magnetic component parameters is analyzed. Fourth, the constraints for optimal magnetic component parameters are derived under variable load conditions to further reduce current stress. Finally, a design process for the optimal inductance and turns ratio is built.

The rest of this article is organized as follows. In Section II, the design objectives are thoroughly analyzed. In Section III, an optimal modulation strategy is derived, considering the impact of the junction capacitors of switching devices, to achieve ZVS under light-load conditions. In Section IV, the design process for the optimal magnetic component parameters is presented. In Section V, the experimental results confirm the theoretical analysis. Finally, Section VI concludes this article.

II. Design Objective Analysis

The topology of the DAB converter is depicted in Fig. 1, which consists of two H-bridges, a series inductor, and a high-frequency transformer, along with two filter capacitors. The

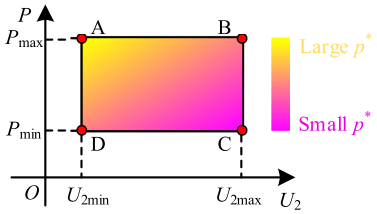

Fig. 2. Given operating condition. Point A represents the operating condition with $U_{2\min}$ and $P_{\max}$. Point B represents the operating condition with $U_{2\max}$ and $P_{\max}$. Point C represents the operating condition with $U_{2\max}$ and $P_{\min}$. Point D represents the operating condition with $U_{2\min}$ and $P_{\min}$. Point A has the maximum per-unit power, while Point C has the minimum per-unit power.

primary bridge, composed of switches S_1–S_4, operates as an inverter, whereas the secondary bridge, consisting of switches Q_1–Q_4, functions as a rectifier. The equivalent inductance L comprises the series inductor and the leakage inductance of the transformer. The transformer can be approximated as an ideal transformer with a turns ratio of n.

A. Inputs and Outputs of the Design Method

Given that magnetic component parameters cannot be altered during operation, they require meticulous design to align with the specific operating conditions. Hence, the input of the design method is the predefined operating condition. The operating conditions defined in this article constitute a variable load condition. This condition encompasses several key parameters, including the input voltage U_1, the switching frequency f_s, the minimum output voltage $U_{2\min}$, the maximum output voltage $U_{2\max}$, the minimum transmission power $P_{\min}$, and the maximum transmission power $P_{\max}$, as depicted in Fig. 2. These conditions are frequently encountered in applications that require efficient energy transfer across a broad range of loads. For example, ON-board chargers and dc chargers for electric vehicles must support various battery voltages while handling different power levels to accommodate varying charging speeds.

There always exists a peak current I_{Lp} corresponding to a specific operating point. The maximum peak current observed across the entire specified operating condition is formally denoted as the current stress I_{Lm}, as depicted in

$$I_{\mathrm{Lm}} = \max_{U_2,P} \left(I_{\mathrm{Lp}}\right). \tag{1}$$

The output of the design method is the optimized magnetic component parameters, specifically the optimal inductance and turns ratio, to minimize the current stress and achieve ZVS or QZVS across the entire given operating condition. It is crucial to emphasize that this proposed method is precisely tailored to meet the predefined operating conditions.

B. Analysis on Peak Current

To minimize the peak current, it is imperative to analyze the factors affecting its magnitude. The operating waveforms of DAB converters are depicted in Fig. 3, where D_1 is the phase-shift ratio between S_1 and S_4, D_2 represents the phase-shift ratio between S_1 and Q_1, D_3 denotes the phase-shift ratio between Q_1 and Q_4, T_{hs} is the half-switching period, and u_{L} is the voltage

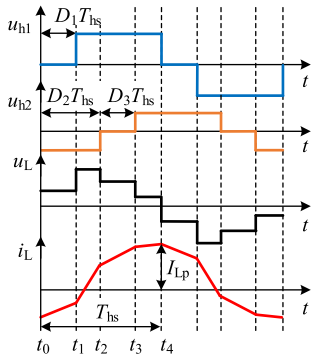

Fig. 3. Operating waveforms of DAB converters under TPS control.

of the inductor, and u_{h1} and u_{h2} represent the output voltages of primary and secondary bridges, respectively. It is evident that the phase-shift ratios will affect the duration of inductor current at each stage [25]. For example, the phase-shift ratio D_1 will affect the duration from t_0 to t_1, and the phase-shift ratio D_3 will affect the duration from t_2 to t_3.

Indeed, magnetic component parameters will influence the slope of inductor current at each stage, as indicated in (2). Therefore, for a specific operating point where the values of U_1, U_2, P, and f_s are all predetermined, the peak current can be mathematically represented as (3)

$$\frac{\mathrm{d}i_{\mathrm{L}}}{\mathrm{d}t} = \frac{u_{\mathrm{h1}} - nu_{\mathrm{h2}}}{L} \tag{2}$$

$$\frac{I_{\mathrm{Lp}}}{I_{\mathrm{in}}} = I^*_{\mathrm{Lp}}\left(D_1, D_2, D_3, n, L\right) \tag{3}$$

where I^*_{Lp} denotes the per-unit value of the peak current I_{Lp}, with the input current I_{in} serving as the base value.

C. Analysis on Soft Switching

The implementation of soft switching is greatly influenced by the operating mode, which depends on the specific operating conditions and magnetic component parameters [17]. Soft switching occurs naturally across most heavy-load modes but poses more challenges in light-load modes. Typically, operating modes can be assessed by the per-unit power p^*. The per-unit power is depicted in (4), with the maximum transmission power $P_{\mathrm{B}} = nU_1U_2/(8f_sL)$ serving as the base value

$$p^* = \frac{P}{P_{\mathrm{B}}} = \frac{8f_sL}{nU_1}\frac{P}{U_2} \tag{4}$$

$$p^*_{\mathrm{C}} \le \frac{p^*_{\mathrm{C}}}{p^*_{\mathrm{A}}} = \frac{P_{\min}}{P_{\max}} \cdot \frac{U_{2\min}}{U_{2\max}}. \tag{5}$$

Under the given operating condition and specific inductance and turns ratio, the maximum and minimum per-unit powers, respectively, correspond to the conditions at Point A and Point C in Fig. 2, as defined by (4). Since p^*_{A} is less than 1, p^*_{C} is impacted by both the output voltage range and the transmission power range, as proven in (5). In the context of broad ranges of output voltage and transmission power, p^*_{C} greatly decreases, potentially affecting the feasibility of soft switching. For example, if the per-unit power is less than $2U_1(nU_2-U_1)/(nU_2)^2$,

full ZVS will be lost with the modulation strategy in [17]. Notably, once the operating conditions are defined, it becomes impractical to substantially increase p_{C}^{*} by adjusting the turns ratio and inductance. This implies that to achieve full ZVS under light-load conditions, the modulation strategy should be optimized.

III. Analysis and Derivation of the Optimal Modulation Strategy

For the specific operating point, and specific inductance and turns ratio, there always exists corresponding optimal phase-shift ratios that can minimize the peak current to the greatest extent and achieve full ZVS, as illustrated in

$$\min_{D_1,D_2,D_3}\left(\frac{I_{\mathrm{Lp}}}{I_{\mathrm{in}}}|_{n,L}\right)=I_{\mathrm{Lp}}^{*}\left(D_{1,\mathrm{opt}},D_{2,\mathrm{opt}},D_{3,\mathrm{opt}}\right) \tag{6a}$$

$$I_{\mathrm{ZVS}}\geq\sqrt{\frac{2C_{\mathrm{oss,eq}}U^{2}}{L}} \tag{6b}$$

where $D_{1,\mathrm{opt}}$, $D_{2,\mathrm{opt}}$, and $D_{3,\mathrm{opt}}$ are the optimal phase-shift ratios, the soft-switching current I_{ZVS} denotes the inductor current to completely discharge the junction capacitors of switching devices during the dead time [32], the voltage U could be either the input voltage U_1 or the output voltage U_2, and $C_{\mathrm{oss,eq}}$ is the equivalent junction capacitance of switching devices.

Hence, the optimization of magnetic component parameters can be refined based on an optimal modulation strategy. The combined approach described herein not only facilitates further reduction in the peak current but also streamlines the representation of the peak current with respect to the magnetic component parameters, as demonstrated in

$$\frac{I_{\mathrm{Lp}}}{I_{\mathrm{in}}}=I_{\mathrm{Lp}}^{*}\left(n,L\right). \tag{7}$$

The derivation of the optimal modulation strategy involves two steps: first, identifying operation modes that achieve ZVS or QZVS over the entire power range, and secondly, utilizing the Karush–Kuhn–Tucker method or global optimal condition (GOC) equations to further reduce the peak current of each mode [33], [12].

A. Operating Modes for Soft Switching

The voltage ratio k is defined as

$$k=\frac{U_1}{nU_2}. \tag{8}$$

The operating modes for soft switching are depicted in Fig. 4, where u'_{h2} equals nu_{h2}. Modes 1 through 3 correspond to the scenarios where $k\geq 1$, while Modes 4 through 6 pertain to situations where $k<1$. Taking the modes of $k>1$ as an example, the soft switching of each mode is analyzed. Mode 1 is characterized as the light-load mode, as shown in Fig. 4(a). Due to the utilization of a three-level configuration in both u_{h1} and u'_{h2}, the actual power is notably lower than its rated power. At time t_1 of Mode 1, Q_4 turns ON. The inductor current discharges the junction capacitor of Q_4 and charges the junction capacitor of Q_3, as shown in Fig. 5(a). After the voltage drop

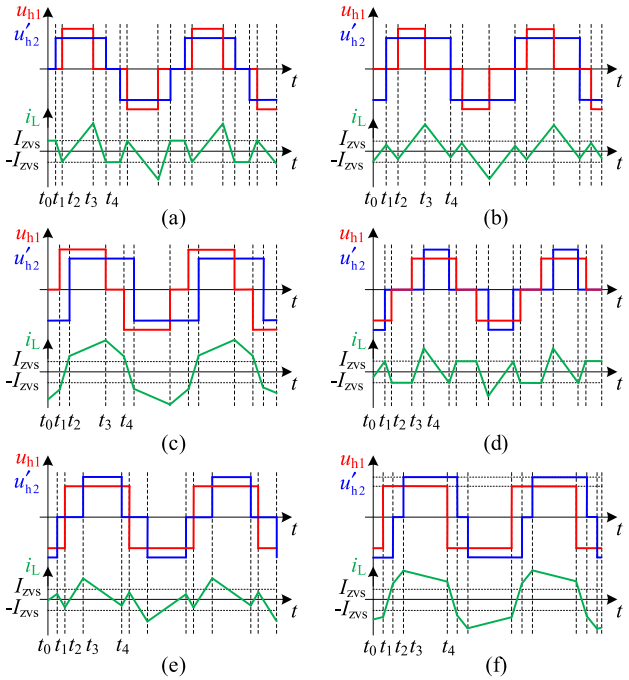

Fig. 4. Operating mode classification of soft switching under TPS control. (a) Mode 1. (b) Mode 2. (c) Mode 3. (d) Mode 4. (e) Mode 5. (f) Mode 6.

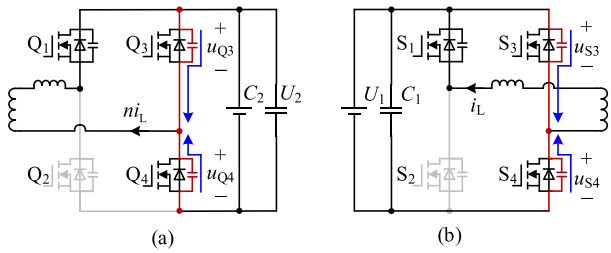

Fig. 5. ZVS performance of DAB converters. (a) ZVS of Q_4. (b) ZVS of S_4.

across the junction capacitor of Q_4 reaches zero, Q_4 turns ON and achieves ZVS. According to (6b), the inductor current at time t_1 is required to fulfill the condition outlined in (9a) to ensure that the voltage drop across the junction capacitor of Q_4 reaches zero. Similarly, during the dead time near t_2, the inductor current discharges and charges the junction capacitors of S_4 and S_3, respectively, as depicted in Fig. 5(b). To achieve soft switching for S_4, the inductor current at time t_2 is required to comply with (9b). To simplify the modulation strategy and ensure that the switches on both the primary and secondary sides achieve ZVS, it is crucial that the amplitudes of the inductor current at t_1 and t_2 both equal the soft-switching current I_{ZVS} in this mode, as described in (10), where the $C_{\mathrm{oss,pri}}$ and $C_{\mathrm{oss,sec}}$ represent the equivalent junction capacitance of the switches on the primary and secondary sides, respectively.

As the transmission power rises, the voltage u'_{h2} gradually transitions from a three-level state to a two-level state, with D_3 reaching zero, as denoted by Mode 2 and shown in Fig. 4(b). In this mode, the phase-shift ratio D_1 consistently decreases as the transmission power rises, resulting in a gradual decrease in the

current values at times t_1 and t_2

$$|i_{\mathrm{L}}(t_1)| \geq \sqrt{\frac{2C_{\mathrm{oss,sec}}U_{2\max}^2}{L}} \tag{9a}$$

$$|i_{\mathrm{L}}(t_2)| \geq \sqrt{\frac{2C_{\mathrm{oss,pri}}U_1^2}{L}} \tag{9b}$$

$$I_{\mathrm{ZVS}} \geq \max\left\{\sqrt{\frac{2C_{\mathrm{oss,pri}}U_1^2}{L}}, \sqrt{\frac{2C_{\mathrm{oss,sec}}U_{2\max}^2}{L}}\right\}. \tag{10}$$

As transmission power continues to rise, the value of D_1 decreases until the turn-ON time of S_4 precedes the turn-ON time of Q_1, as observed in Mode 3. In this mode, the current values at t_1 and t_2 increase with the surge in power, allowing full soft-switching to be naturally achieved across most of Mode 3. It is noteworthy that, in the transition region between Mode 2 and Mode 3, the inductor current values at t_1 and t_2 are very small. Considering the influence of junction capacitors, the inductor current at these points may drop below the minimum required for discharging the junction capacitor. Consequently, in the transition region between Mode 2 and Mode 3, some switches may achieve QZVS rather than ZVS.

It is crucial to note that the soft-switching current I_{ZVS} is affected by the inductance L, as shown in (10). Characterizing the optimal modulation strategy using I_{ZVS} adds complexity to the subsequent optimization of magnetic component parameters, as it necessitates accounting for the influence of L on I_{ZVS}. To mitigate this, the soft-switching factor G_{ZVS} is introduced, as defined in (11). To ensure full soft switching under light-load conditions, G_{ZVS} must satisfy the condition outlined in (12), as derived from (10)

$$G_{\mathrm{ZVS}} = I_{\mathrm{ZVS}}\sqrt{\frac{8f_{\mathrm{s}}L}{P}} \tag{11}$$

$$G_{\mathrm{ZVS}} \geq \max\left\{4\sqrt{\frac{f_{\mathrm{s}}U_1^2C_{\mathrm{oss,pri}}}{P_{\min}}}, 4\sqrt{\frac{f_{\mathrm{s}}U_{2\max}^2C_{\mathrm{oss,sec}}}{P_{\min}}}\right\}. \tag{12}$$

To simplify the modulation strategy, a fixed value for soft-switching factor G_{ZVS} can be adopted. In practical applications, DAB converters often run in high-voltage and high-power scenarios, with parameters such as a switching frequency of 20 kHz, an input voltage of 1 kV, a maximum output voltage of 1 kV, a minimum transmission power of 1 kW, an equivalent junction capacitance of 300 pF, and a turns ratio of 1. According to (12), ensuring G_{ZVS} is greater than 0.31 guarantees ZVS for all switches. In this study, G_{ZVS} is defined as 0.5.

B. Modulation Strategy for Minimum Peak Current

The peak current for each mode needs to be optimized to obtain the optimal modulation strategy. Mode 1 possesses three degrees of freedom and simultaneously accommodates three constraints, including t_1, the requirement that the current value at t_2 equals I_{ZVS}, and the transmission power. Therefore, Mode 1 lacks additional degrees of freedom for optimizing the peak current. Mode 2 has two degrees of freedom along with two accompanying constraints, which include the transmission power and the mandated shift between modes. Hence, Mode 2 cannot further optimize the peak current. As the transmission power increases, full ZVS can be naturally achieved across most of Mode 3. Therefore, Mode 3 frees up a degree of freedom optimized for peak current. The phase-shift constraints for each mode are then optimized, and a control method for the modulation strategy is developed.

1) Mode 1: Based on the periodic symmetry of the inductor current, the inductor current at times t_1 and t_2, as well as the transmission power P in Mode 1, can be derived, as shown in (13). To achieve full ZVS, the inductor current at t_1 and t_2 is set to I_{ZVS} and $-I_{\mathrm{ZVS}}$, respectively, as illustrated in Fig. 4(a)

$$\begin{cases} i_{\mathrm{L}}(t_1) = \frac{nU_2}{4f_{\mathrm{s}}L}\left[1 - D_3 - k(1-D_1)\right] \\ i_{\mathrm{L}}(t_2) = \frac{nU_2}{4f_{\mathrm{s}}L}\left[2D_2 - 2D_1 + D_3 + 1 - k(1-D_1)\right] \\ P = \frac{nU_1U_2}{4f_{\mathrm{s}}L}(1-D_1)(2D_2 - D_1 + D_3). \end{cases} \tag{13}$$

Building upon the three constraint conditions outlined in (13), the phase-shift ratios are optimized. To circumvent the use of I_{ZVS}, which is influenced by the inductance L, the soft-switching factor G_{ZVS} is introduced as a substitute, as defined in (11). The optimized phase-shift ratios are provided in (14).

$$\begin{cases} D_1 = 1 - \frac{\sqrt{p^*\left(kG_{\mathrm{ZVS}}^2 + 8k - 8\right)} + G_{\mathrm{ZVS}}\sqrt{kp^*}}{4k-4} \\ D_2 = \frac{p^*}{4(1-D_1)} + \frac{1}{2}(D_1 - D_3) \\ D_3 = 1 - k(1-D_1) - \frac{G_{\mathrm{ZVS}}\sqrt{kp^*}}{2}. \end{cases} \tag{14}$$

2) Mode 2: According to Fig. 4(b), the transmission power in Mode 2 can be derived, as expressed in (15). To ensure continuity of the phase-shift ratios between Mode 1 and Mode 2, the phase-shift ratio D_2 in Mode 2 is set to match that of Mode 1. Given that $D_3 = 0$, the phase-shift ratios for Mode 2 can be designed based on these two constraints, as presented in (16)

$$P = \frac{nU_1U_2}{4f_{\mathrm{s}}L}(1-D_1)(2D_2 - D_1) \tag{15}$$

$$\begin{cases} D_1 = 1 - \frac{1 + \sqrt{4kp^* - 2p^* + 1}}{4k-2} \\ D_2 = \frac{p^*}{4(1-D_1)} + \frac{1}{2}(D_1 - D_3) \\ D_3 = 0. \end{cases} \tag{16}$$

3) Mode 3: According to Fig. 4(c), the peak current I_{Lp} and transmission power P in Mode 3 can be derived, as given in (17). Using the GOC equations [12], the phase-shift ratios for minimizing the peak current can be determined by ensuring that the phase-shift ratio constraint satisfies (18), as outlined in (19)

$$\begin{cases} I_{\mathrm{Lp}} = i_{\mathrm{L}}(t_3) = \frac{nU_2}{4f_{\mathrm{s}}L}\left[2D_2 - 1 + k(1-D_1)\right] \\ P = \frac{nU_1U_2}{4f_{\mathrm{s}}L}\left(2D_1D_2 + 2D_2 - D_1^2 - 2D_2^2 - D_1\right) \end{cases} \tag{17}$$

$$\frac{\partial I_{\mathrm{Lp}}}{\partial D_1} : \frac{\partial P}{\partial D_1} = \frac{\partial I_{\mathrm{Lp}}}{\partial D_2} : \frac{\partial P}{\partial D_2} \tag{18}$$

$$\begin{cases} D_1 = (k-1)\sqrt{\frac{1-p^*}{k^2-2k+2}} \\ D_2 = \frac{k - (D_1+1)}{2(k-1)} + \frac{D_1 - D_3}{2} \\ D_3 = 0. \end{cases} \tag{19}$$

TABLE I
BOUNDARIES AMONG EACH MODE

	p^*_{bo1}	p^*_{bo2}
$0<k\le 1$	$\dfrac{k\left[\left(4G_{\mathrm{ZVS}}k-6G_{\mathrm{ZVS}}\right)\sqrt{G_{\mathrm{ZVS}}^2-8k+8}+\left(4k^2-12k+10\right)G_{\mathrm{ZVS}}^2+8-8k\right]}{\left(G_{\mathrm{ZVS}}^2k-2G_{\mathrm{ZVS}}^2+2\right)^2}$	$2k-2k^2$
$k>1$	$\dfrac{\left(4G_{\mathrm{ZVS}}-6G_{\mathrm{ZVS}}k\right)\sqrt{k^2G_{\mathrm{ZVS}}^2+8k^2-8k}+\left(10k^2-12k+4\right)G_{\mathrm{ZVS}}^2+8k^2-8k}{k\left(G_{\mathrm{ZVS}}^2-2G_{\mathrm{ZVS}}^2k+2k\right)^2}$	$\dfrac{2k-2}{k^2}$

TABLE II
OPTIMAL PHASE-SHIFT RATIOS OF EACH MODE

	$p^*\in\left(0,p^*_{\mathrm{bo1}}\right)$	$p^*\in\left[p^*_{\mathrm{bo1}},p^*_{\mathrm{bo2}}\right)$	$p^*\in\left[p^*_{\mathrm{bo2}},1\right)$
	Mode 1	Mode 2	Mode 3
$0<k\le 1$	$D_1=1-\dfrac{1-D_3}{k}-\dfrac{G_{\mathrm{ZVS}}\sqrt{kp^*}}{2k}$ $D_2=\dfrac{p^*}{4(1-D_3)}+\dfrac{1}{2}(D_1-D_3)$ $D_3=1-\dfrac{\sqrt{p^*\left(kG_{\mathrm{ZVS}}^2-8k^2+8k\right)}+G_{\mathrm{ZVS}}\sqrt{kp^*}}{4-4k}$	$D_1=0$ $D_2=\dfrac{p^*}{4(1-D_3)}+\dfrac{1}{2}(D_1-D_3)$ $D_3=1-\dfrac{k+\sqrt{k^2-2k^2p^*+4kp^*}}{4-2k}$	$D_1=0$ $D_2=\dfrac{1-k(D_3+1)}{2(1-k)}+\dfrac{D_1-D_3}{2}$ $D_3=(1-k)\sqrt{\dfrac{1-p^*}{2k^2-2k+1}}$
	Mode 4	Mode 5	Mode 6
$k>1$	$D_1=1-\dfrac{\sqrt{p^*\left(kG_{\mathrm{ZVS}}^2+8k-8\right)}+G_{\mathrm{ZVS}}\sqrt{kp^*}}{4k-4}$ $D_2=\dfrac{p^*}{4(1-D_1)}+\dfrac{1}{2}(D_1-D_3)$ $D_3=1-k(1-D_1)-\dfrac{G_{\mathrm{ZVS}}\sqrt{kp^*}}{2}$	$D_1=1-\dfrac{1+\sqrt{4kp^*-2p^*+1}}{4k-2}$ $D_2=\dfrac{p^*}{4(1-D_1)}+\dfrac{1}{2}(D_1-D_3)$ $D_3=0$	$D_1=(k-1)\sqrt{\dfrac{1-p^*}{k^2-2k+2}}$ $D_2=\dfrac{k-(D_1+1)}{2(k-1)}+\dfrac{D_1-D_3}{2}$ $D_3=0$

4) Boundary Design: From Fig. 4(a), as transmission power increases, D_3 in Mode 1 decreases, and u_{h2} transitions from a three-level state to a two-level state to enhance the power absorption on the output side. Thus, the boundary condition between Mode 1 and Mode 2 is $D_3 = 0$. Similarly, as the transmission power continues to rise, the phase-shift ratio D_1 in Mode 2 decreases, while D_2 increases, thereby boosting the power delivered from the input side. The boundary condition between Mode 2 and Mode 3 is $D_1 = D_2$. By substituting these boundary conditions into (14) and (16), respectively, the per-unit powers at the boundary conditions, $p^*_{\mathrm{bo1}}$and p^*_{bo2}, can be obtained, as shown in Table I.

The analysis method for the voltage ratio $k < 1$ is similar. Tables II and III summarize the optimal phase-shift ratios and minimum peak current for each mode. From Table II, the variation of the phase-shift ratios with respect to the per-unit power can be derived, as shown in Fig. 6.

5) Control Method: The control diagram of the proposed modulation strategy is depicted in Fig. 7. The input and output voltages, U_1 and U_2, are sampled to design the voltage ratio k. The difference between the reference output voltage $U_{2\mathrm{ref}}$ and U_2 is processed by a proportional-integral controller to generate the per-unit power p^*. The phase-shift ratios are then designed based on Tables I and II. Finally, the gate signals are generated.

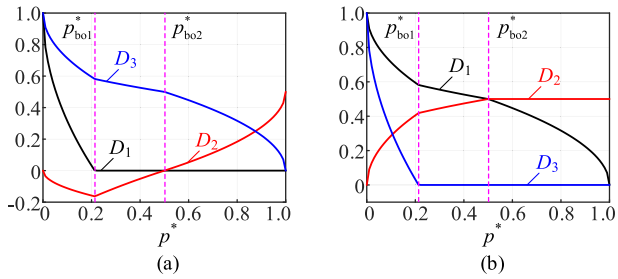

Fig. 6. Variation of phase-shift ratios with per-unit power. (a) $k = 0.5$. (b) $k = 2$.

TABLE III
MINIMUM PEAK CURRENT OF EACH MODE

Mode 1	Mode 2	Mode 3
$I_{Lp}^{*}=\frac{\sqrt{p^{*}\left(kG_{ZVS}^{2}-8k^{2}+8k\right)}}{p^{*}}$	$I_{Lp}^{*}=\frac{(3-2k)\sqrt{4kp^{*}-2k^{2}p^{*}+k^{2}}-k}{p^{*}(2-k)}$	$I_{Lp}^{*}=\frac{2-2\sqrt{(1-p^{*})(2k^{2}-2k+1)}}{p^{*}}$
Mode 4	**Mode 5**	**Mode 6**
$I_{Lp}^{*}=\frac{\sqrt{p^{*}\left(G_{ZVS}^{2}k+8k-8\right)}}{p^{*}}$	$I_{Lp}^{*}=\frac{(3k-2)\sqrt{4kp^{*}-2p^{*}+1}-k}{p^{*}(2k-1)}$	$I_{Lp}^{*}=\frac{2k-2\sqrt{(1-p^{*})(k^{2}-2k+2)}}{p^{*}}$

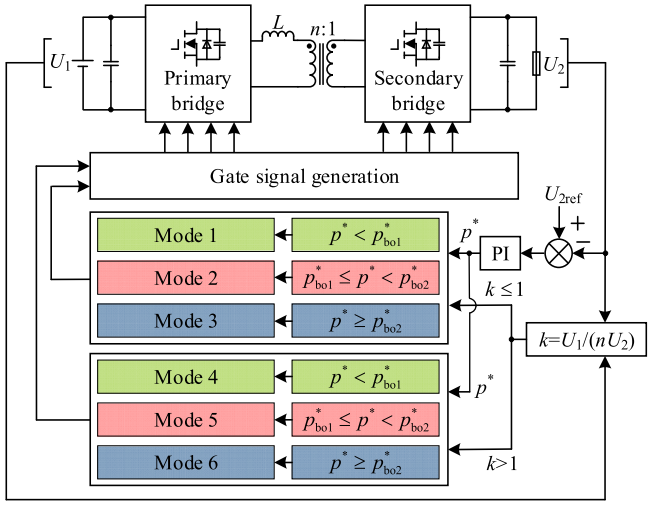

Fig. 7. Control diagram of the proposed modulation strategy.

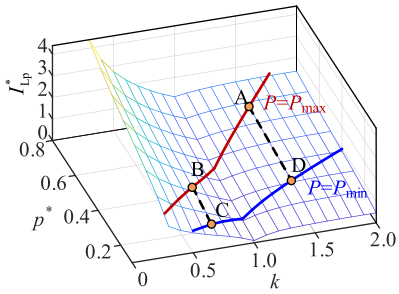

Fig. 8. Per-unit peak current with respect to p^* and k.

IV. DESIGN METHOD OF MAGNETIC COMPONENT PARAMETERS

Based on Tables I and III, a three-dimensional surface of the per-unit peak current I_{Lp}^{*} with respect to the per-unit power p^* and voltage ratio k can be generated, as shown in Fig. 8, where the region of A-B-C-D represents the peak current under given operating conditions in Fig. 2. Since the current stress always occurs under the conditions with the maximum transmission power P_{max}, it is critical to reduce the peak current along segments from A to B by optimizing the magnetic parameters.

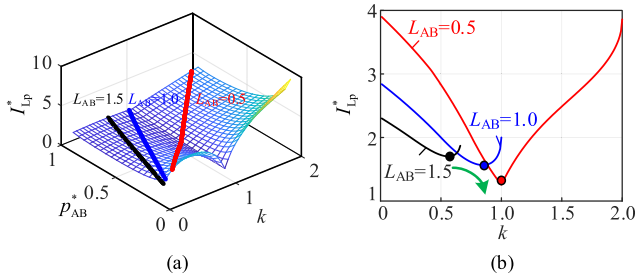

Fig. 9. (a) Surface of peak current varying with p^*_{AB} and k under different L_{AB}. (b) Curves of peak current varying with k under different L_{AB}.

According to (8), the value of k will vary within the range of $k_{min} = U_1/(nU_{2max})$ to $k_{max} = U_1/(nU_{2min})$ for a given operating condition. The relationship between k and p^* along segments from A to B can be deduced from (4) and (8), as shown in (20), where p^*_{AB} denotes the per-unit power along this segment, and L_{AB} represents the slope of the per-unit power p^*_{AB}

$$p^*_{AB}=\frac{8f_sP_{max}L}{U_1^2}k=L_{AB}k. \tag{20}$$

Under given operating conditions, k_{min} represents the turns ratio n according to $k_{min} = U_1/(nU_{2max})$, and L_{AB} denotes the inductance L according to (20). Hence, the optimization of magnetic component parameters is equivalent to identifying the optimal combination of L_{AB} and k_{min} for the minimum current stress along the segment from A to B.

A. Effect of L_{AB} on the Current Stress

The effect of L_{AB} on the peak current is depicted in Fig. 9. Since p^* must be less than 1, the greater the value of L_{AB}, the smaller the range of k, based on (20). If the range of k departs from $k = 1$, it leads to an increase in the backflow power, thereby decreasing the efficiency. Therefore, there arises a necessity to constrain the value of L_{AB}. It can be observed from Fig. 9(b) that an increase in L_{AB} results in the leftward displacement of the minimum point, where the maximum p^*_{AB} is set to 1. This article constrains L_{AB} by maintaining the minimum point at $k = 1$. Consequently, the condition that $L_{AB} \le 0.83$ can be determined by deriving the peak currents of Mode 3 and Mode 6.

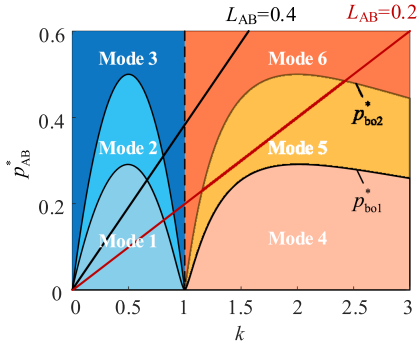

Fig. 10. Operating zones of each mode. Black curve is the operating modes with $L_{AB} = 0.4$. Red curve is the operating modes with $L_{AB} = 0.2$.

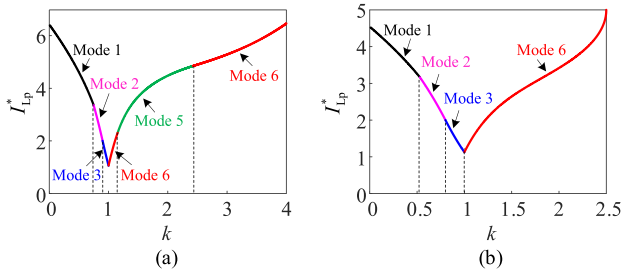

Fig. 11. (a) Modes of peak current with $L_{AB} = 0.2$. (b) Modes of peak current with $L_{AB} = 0.4$.

According to Table I, the operating zones of each mode are, as depicted in Fig. 10, where L_{AB} will affect the mode selection. When L_{AB} is small, Modes 4, 5, and 6 may all occur on the $k>1$ side, as depicted in Fig. 11(a). As L_{AB} increases, the variety of modes appearing on the $k>1$ side decreases until only Mode 6 remains, as shown in Fig. 11(b). Given that L_{AB} is proportional to the inductance L, an increase in L_{AB} results in a reduction in peak current. Therefore, consideration is limited to scenarios in which only Mode 6 manifests on the $k>1$ side. By deriving the boundary conditions between Mode 5 and Mode 6, L_{AB} is finally constrained within the range from 0.3 to 0.83.

B. Effect of k_{min} on the Current Stress

To standardize the output voltage range, the ratio of the maximum output voltage $U_{2\max}$ to the minimum output voltage $U_{2\min}$ is defined as the output voltage range and denoted as λ, as shown in

$$\lambda = \frac{U_{2\max}}{U_{2\min}} = \frac{k_{\max}}{k_{\min}}. \tag{21}$$

The effect of distributions of k on the current stress is shown in Fig. 12, where $k_{1\max}/k_{1\min} = k_{2\max}/k_{2\min}$ represents the same output voltage range. The current stress is consistently lower when $I_{Lp}(k_{\min})$ equals $I_{Lp}(k_{\max})$ compared to that when they are unequal. Thus, the constraint for $k_{\min}$ and $k_{\max}$ meets (22). In this case, the peak currents of $k_{\min}$ and $k_{\max}$ are the current stress I_{Lm}

$$I_{Lm} = I_{Lp}(k_{\min}) = I_{Lp}(k_{\max}). \tag{22}$$

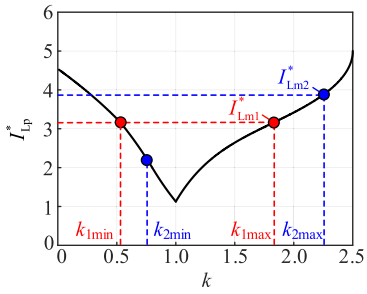

Fig. 12. Effect of distributions of $k_{\min}$ and $k_{\max}$ on the current stress.

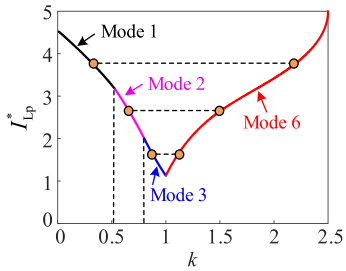

Fig. 13. Effect of output voltage range on the current stress.

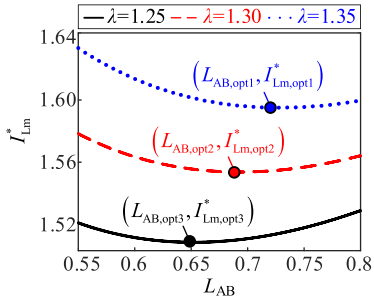

Fig. 14. Optimal L_{AB} values across various output voltage ranges.

C. Optimal L_{AB} and k_{min}

The distributions of k with different output voltage ranges are shown in Fig. 13. In cases of a narrow output voltage range, the operating point at $k_{\min}$ resides in Mode 3. With an expanded output voltage range, the operating point at $k_{\min}$ shifts to Mode 2 or Mode 1. It is noteworthy that the mode in which $k_{\min}$ operates has an impact on (22).

In cases of a narrow output voltage range, $k_{\min}$ operates in Mode 3, and (22) can be expressed as (23). The relationship between $k_{\min}$ and λ can be obtained from (23), yielding (24). Substituting (24) into the peak current in Mode 3 yields (25), where the current stress I_{Lm} is determined solely by L_{AB} and λ. As a result, within a specific output voltage range λ, an optimal L_{AB} exists that minimizes the current stress, as depicted in Fig. 14, where $L_{AB,opt\,i}$ and $I^*_{Lm,opt\,i}$ ($i = 1, 2, 3$), respectively, represent the optimal L_{AB} and the optimal per-unit current stress in their corresponding output voltage ranges. To ensure that the system maintains regulation capability at the rated power, the maximum p^* is limited to 0.9. For a given value of λ, $L_{AB,opt}$ can be determined by taking the derivative of (25). This process can

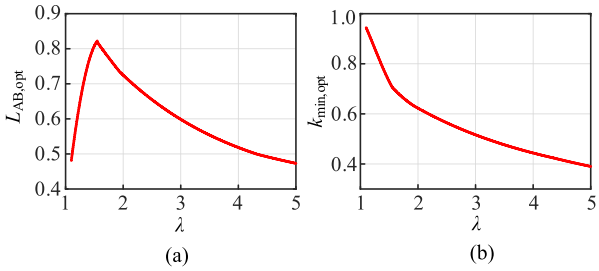

Fig. 15. (a) Curve of the $L_{\mathrm{AB,opt}}$ with respect to the output voltage range λ. (b) Curve of $k_{\mathrm{min,opt}}$ with respect to the output voltage range λ.

be repeated for various λ values. Similarly, when k_{min} operates in Mode 1 or Mode 2, a relationship between L_{AB} and λ for the current stress I_{Lm} can be established, and an optimal L_{AB} for a specific output voltage range λ can be obtained

$$I_{\mathrm{Lm}} = I_{\mathrm{Lp}}\left(k_{\mathrm{min}}\right)|_{\mathrm{Mode3}} = I_{\mathrm{Lp}}\left(k_{\mathrm{max}}\right)|_{\mathrm{Mode6}} \tag{23}$$

$$k_{\mathrm{min}} = f\left(L_{\mathrm{AB}}, \lambda\right) \tag{24}$$

$$I_{\mathrm{Lm}} = h\left(L_{\mathrm{AB}}, \lambda\right). \tag{25}$$

The corresponding optimal L_{AB} for various output voltage ranges λ can be depicted in Fig. 15(a). To determine $L_{\mathrm{AB,opt}}$ for a specific value of λ, a polynomial function is fitted to the data presented in Fig. 15(a), as illustrated in (26). Notably, when $L_{\mathrm{AB,opt}}$ is established, the optimal k_{min}, $k_{\mathrm{min,opt}}$, can be uniquely defined as well. By substituting (26) into (24), the variation of $k_{\mathrm{min,opt}}$ concerning λ is represented in Fig. 15(b). A polynomial function is fitted to the data in Fig. 15(b) to ascertain $k_{\mathrm{min,opt}}$ for a given λ value, as indicated in (27)

$$L_{\mathrm{AB,opt}} = \begin{cases} -1.193\lambda^2 + 3.919\lambda - 2.386 & \lambda \le 1.55 \\ -0.006439\lambda^3 + 0.0895\lambda^2 - 0.4618\lambda + 1.341 & \lambda > 1.55 \end{cases} \tag{26}$$

$$k_{\mathrm{min,opt}} = \begin{cases} 0.5442\lambda^3 - 2.03\lambda^2 + 1.96\lambda + 0.5088 & \lambda \le 1.55 \\ -0.005758\lambda^3 + 0.07529\lambda^2 - 0.3833\lambda + 1.131 & \lambda > 1.55 \end{cases}. \tag{27}$$

D. Design Process

The design process can be divided into 4 steps, as depicted in Fig. 16, where L_{opt} represents the optimal inductance L and n_{opt} represents the optimal turns ratio n. The first step is to determine the given operating condition. The second step is to calculate the output voltage range λ. The third step is to determine the optimal L_{AB} and k_{min} according to (26) and (27). Finally, the optimal inductance and turns ratio that minimize the current stress can be obtained.

Since the maximum per-unit power value is limited to 0.9, the power margin of the proposed method is 10%. When the converter hardware is well-designed, maintaining the magnetic component parameters specified in Fig. 16 minimizes current stress to the greatest extent. However, when the converter

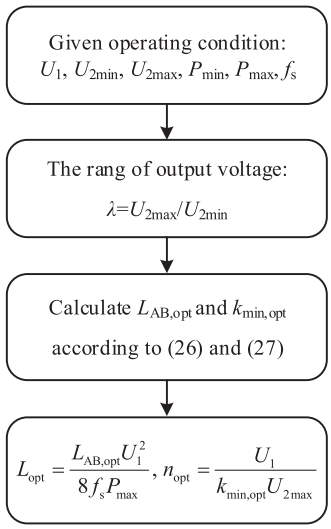

Fig. 16. Design process for the optimal inductance and turns ratio.

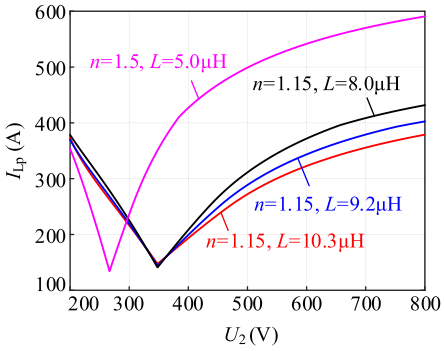

Fig. 17. Effect of fine-tuning the inductance on peak currents.

hardware design is suboptimal, such as when low-performance switching devices or poor magnetic component manufacturing are used, the increased losses and a reduced power margin may limit the ability to increase input power and adjust the output power to the rated value. In such cases, engineers can fine-tune the inductance while keeping the optimal turns ratio to further increase the power margin. For example, in a typical dc fast charger, the operating conditions are set as follows: $U_1 = 400$ V, $U_{2\mathrm{min}} = 200$ V, $U_{2\mathrm{max}} = 800$ V, $P_{\mathrm{min}} = 10$ kW, $P_{\mathrm{max}} = 50$ kW, $f_s = 20$ kHz. Based on the magnetic component parameters designed in Fig. 16, we have $n_{\mathrm{opt}} = 1.15$ and $L_{\mathrm{opt}} = 10.3$ μH, yielding a power margin of 10%. By keeping the optimal turns ratio fixed and reducing the inductance, the power margin can be increased. Specifically, to achieve power margins of 20% and 30%, the required inductance values are 9.2 μH and 8.0 μH, respectively. Fig. 17 illustrates the peak current at maximum power with the adjusted inductance values where $n = 1.5$ and $L = 5.0$ μH represent the nonoptimized magnetic component parameters. It is noted that although this adjustment slightly increases the peak current, the overall peak current remains relatively low compared to the nonoptimized magnetic component parameters.

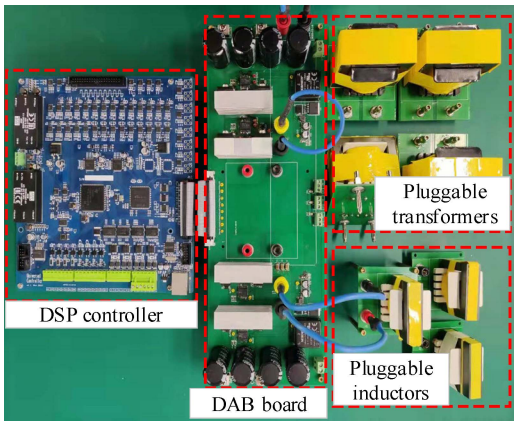

Fig. 18. Experimental prototype of DAB converters.

TABLE IV
GIVEN OPERATING CONDITION

Items	Symbol	Parameters
Input voltage	U_1	100 V
Minimum output voltage	$U_{2\min}$	50 V
Maximum output voltage	$U_{2\max}$	200 V
Minimum transmission power	$P_{\min}$	100 W
Maximum transmission power	$P_{\max}$	400 W
Switching frequency	f_s	50 kHz

V. EXPERIMENTAL RESULTS

To validate the theoretical analysis, an experimental platform has been built, as shown in Fig. 18, incorporating pluggable transformers and inductors. The switches on the primary and secondary sides are IRFB4115PbF and IRFP4137PbF, with equivalent junction capacitances of 490 pF and 300 pF, respectively. The filter capacitors on the primary and secondary sides are 880 μF and 1880 μF, respectively. The current stress and efficiency associated with different magnetic component parameters can be systematically compared through the substitution of various transformers and inductors.

The optimal magnetic component parameters of the specific operating condition listed in Table IV can be designed based on the guidance provided in Fig. 16, resulting in an inductance value of 32.4 μH and a turns ratio of 1.15. Both the transformer and inductor employ Ferrite PC95 as the core material. The core structures, as determined by the area product method, are EE65 for the transformer and EI50 for the inductor, respectively. The transformer is constructed using sandwich-winding techniques with a turns ratio of 46:40 to reduce its ac resistance. The inductors are characterized by the inclusion of an air gap formed through the stacking of 0.1 mm thick polyethylene terephthalate sheets. This design facilitates flexible adjustments of inductance.

TABLE V
SPECIFIC OPERATING CONDITIONS OF 4 OPERATING POINTS

Operating point	U_2/V	P/W	$(D_{1,\text{opt}}, D_{2,\text{opt}}, D_{3,\text{opt}})$	I_{Lp}/A (S)	I_{Lp}/A (E)
A	50	400	(0.187, 0.467, 0)	11.97	12.20
B	200	400	(0, 1.837, 0.636)	12.08	12.00
C	200	100	(0.483, -0.09, 0.814)	6.07	5.90
D	50	100	(0.505, 0.366, 0)	5.27	5.30

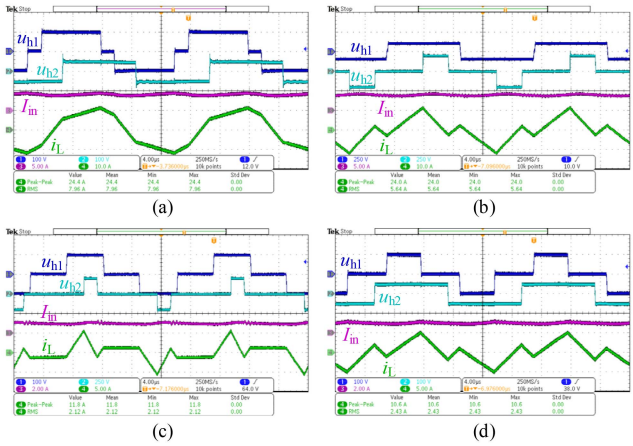

Fig. 19. Experimental waveforms for (a) Point A, where $U_2 = 50$ V and $P = 400$ W, (b) Point B, where $U_2 = 200$ V and $P = 400$ W, (c) Point C, where $U_2 = 200$ V and $P = 100$ W, (d) Point D, where $U_2 = 50$ V and $P = 100$ W.

It is noteworthy that G_{ZVS} should exceed 0.31 according to (12) to guarantee ZVS for all switches, particularly in light-load conditions. The selected value of G_{ZVS} is set as 0.5, which satisfies the given operating conditions.

The operating conditions corresponding to the four operating points in Fig. 2, denoted as Points A, B, C, and D, are detailed in Table V. Additionally, the experimental waveforms are presented in Fig. 19. The peak currents obtained by the experiment (E) are close to the simulation (S) results.

A. Soft Switching Validity

The proposed method facilitates full ZVS under light-load conditions. According to (11), when the soft-switching factor G_{ZVS} is fixed, the soft-switching current I_{ZVS} decreases as the transmission power P is reduced. Furthermore, the energy needed to achieve ZVS increases with the output voltage. As a result, Point C, characterized by the lowest transmission power and the highest output voltage, represents the most challenging condition for achieving full ZVS. This point serves as a benchmark for evaluating the capability of the proposed method to maintain full ZVS under light-load conditions.

Since the two switches in the same bridge leg operate complementarily, they exhibit identical soft-switching behaviors. The soft-switching performances of switches in different bridge legs at Point C are depicted in Fig. 20, where v_{DS} and v_{GS} denote the drain-source voltage and drive voltage, respectively. As observed, the drive voltage rises only after the drain-source

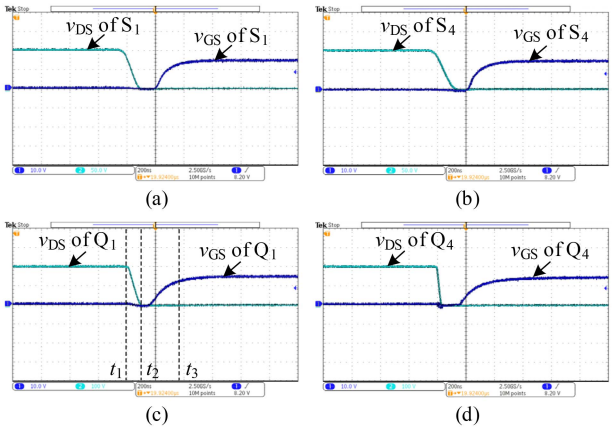

Fig. 20. Soft-switching waveforms for (a) S_1, (b) S_4, (c) Q_1, and (d) Q_4.

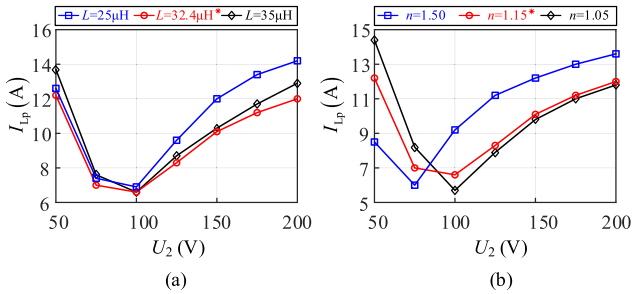

Fig. 21. Comparison of current stresses with different magnetic component parameters. (a) Peak currents with different inductances and the same turns ratio. (b) Peak currents with different turns ratios and the same inductance.

voltage has been discharged to zero, ensuring that all switches achieve ZVS. As an example, the soft-switching process of switch Q_1 is shown in Fig. 20(c). From t_1 to t_2, the inductor current discharges into the junction capacitor of Q_1. From t_2 to t_3, the inductor current commutates to the parallel diode of Q_1. At t_3, the drive voltage of Q_1 rises to its threshold, causing Q_1 to turn ON at zero voltage, thereby achieving ZVS.

B. Comparison With Other Parameters

To verify the capability of the designed magnetic component parameters in reducing the current stress, it is imperative to compare current stresses across different magnetic component parameters. In fact, it is not feasible to measure the current stresses corresponding to all magnetic component parameters. Therefore, a controlled variable method is employed, either by maintaining the turns ratio while altering the inductance, or by keeping the inductance while varying the turns ratio.

It is worth mentioning that each transformer has different leakage inductance. Substituting transformers will introduce alterations in the equivalent inductance. This variation can be alleviated by fine-tuning the inductance gap to ensure the preservation of equivalent inductance. The current stresses corresponding to various inductances and turns ratios are illustrated in Fig. 21. The designed magnetic component parameters, denoted by the symbol "$*$", consistently yield the minimum current stress, thereby validating the effectiveness of the proposed method.

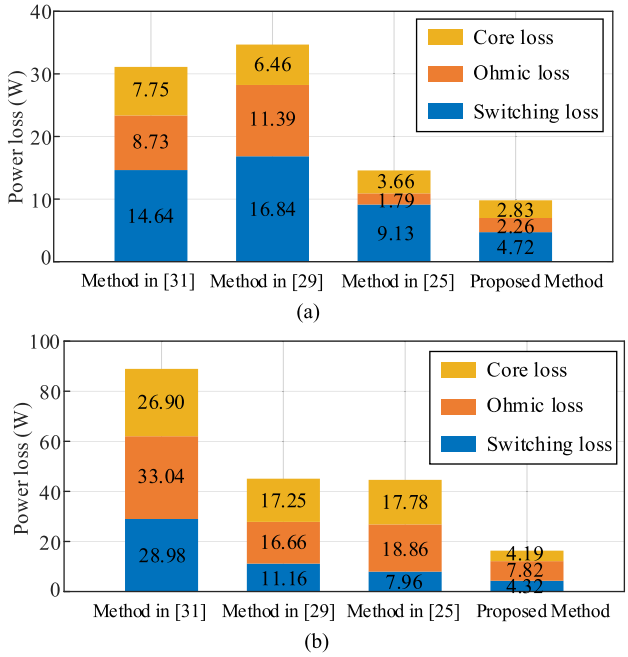

Fig. 22. Loss distributions for different methods under (a) light-load conditions and (b) heavy-load conditions.

C. Loss Analysis and Efficiency Comparison

To validate the superiority of the proposed method on efficiency improvement, a comparative analysis is conducted against other methods. The magnetic component parameters devised through the methods outlined in [25], [29], and [31] under the conditions listed in Table IV are as follows: for [25], $n = 27/36$, $L = 13.0$ μH; for [29], $n = 32/40$, $L = 21.9$ μH; and for [31], $n = 44/20$, $L = 20.7$ μH. To better demonstrate the achievement of full ZVS and the role of optimizing peak current and rms current in reducing losses and enhancing efficiency, Fig. 22 presents the loss distributions for different methods under light-load conditions and heavy-load conditions. Under light-load conditions, the output voltage is 200 V, and the transmission power is 100 W. Under heavy-load conditions, the output voltage is 100 V, and the transmission power is 400 W. The power loss in the DAB converter primarily includes the switching loss, core loss, and ohmic loss. The switching losses consist of the loss due to the overlap of current and voltage, junction capacitor loss, and reverse recovery loss of the body diode [34], which can be calculated using the switching transient waveforms and relevant data from the datasheet. Core losses arise from the changing magnetic flux within the cores and can be approximately calculated using the improved generalized Steinmetz equation [35]. Ohmic losses are mainly composed of the conduction losses in switches and the copper losses in magnetic components. The ON-state resistance of the MOSFET can be obtained from the datasheet, while the ac resistance of the inductor and transformer windings can be calculated using Dowell's equation [36].

According to the loss breakdown depicted in Fig. 22, it can be observed that under light-load conditions, switching losses are the dominant component. The proposed method enables full

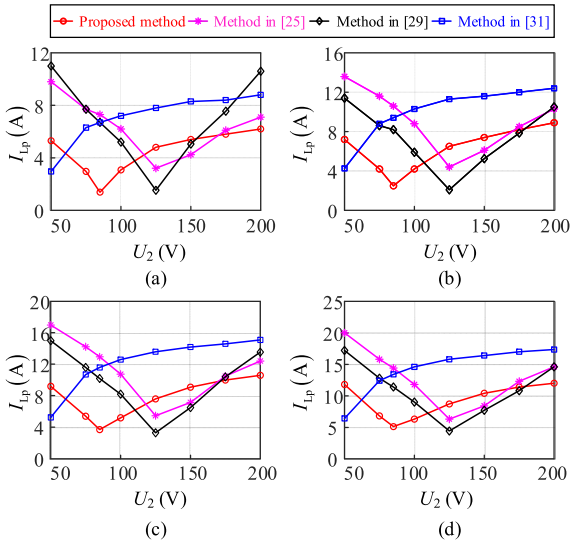

Fig. 23. Comparison of the proposed method and existing methods on the peak current under the condition with (a) 100 W transmission power, (b) 200 W transmission power, (c) 300 W transmission power, and (d) 400 W transmission power.

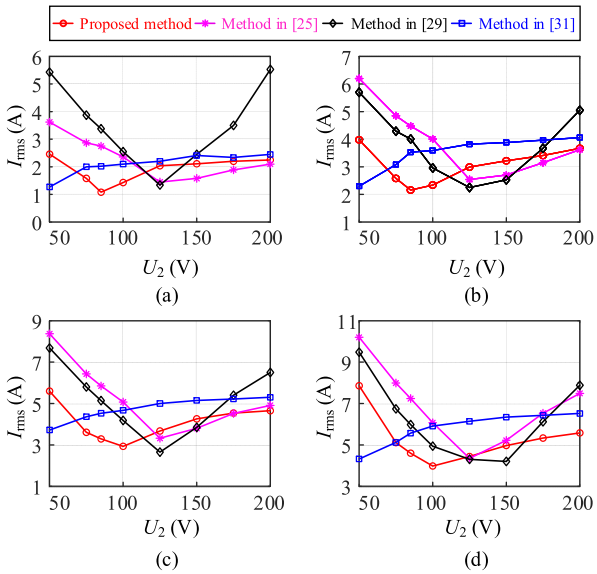

Fig. 24. Comparison of the proposed method and existing methods on the rms current under the condition with (a) 100 W transmission power, (b) 200 W transmission power, (c) 300 W transmission power, and (d) 400 W transmission power.

ZVS under light-load conditions, significantly reducing switching losses, thereby improving system efficiency. In contrast, under heavy-load conditions, copper losses, and core losses dominate. The proposed method effectively suppresses both the peak current and rms current, thus significantly reducing copper losses and core losses, which leads to a notable improvement in efficiency.

In order to obtain more comprehensive comparative results, experiments are conducted under various conditions. The experimental results for the peak current, rms current and efficiency

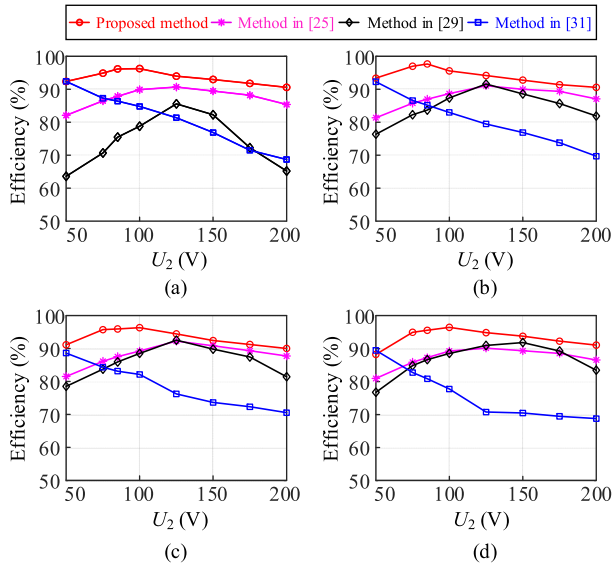

Fig. 25. Comparison of the proposed method and existing methods on the efficiency under the condition with (a) 100 W transmission power, (b) 200 W transmission power, (c) 300 W transmission power, and (d) 400 W transmission power.

of various methods are, respectively, depicted in Figs. 23, 24, and 25, where $I_{\rm rms}$ denotes the rms current.

The experimental results indicate that the proposed method exhibits the minimum current stress across various loads.

Moreover, within the specified operating condition, both the peak current and rms current of the proposed method are generally lower than those of other methods. This highlights an overall optimization achieved by the proposed method in terms of both the peak current and rms current. Under heavy-load conditions, where the output voltage is low and the output current is high, the proposed method demonstrates significantly lower peak current and rms current compared to other methods. Additionally, under light-load conditions, where the output voltage is high and the output current is low, the proposed method leverages the advantages of full ZVS. This combination results in the efficiency of the proposed method being higher than that of other methods across the entire power range. As the transmission power increases, the proposed method generally demonstrates lower peak current and rms current compared to other methods, thereby maintaining an efficiency advantage, as depicted in Fig. 25.

VI. Conclusion

In this article, a novel efficiency optimization strategy that integrates both modulation strategy optimization and magnetic component parameter optimization is proposed, significantly enhancing efficiency. The optimal modulation strategy is derived to achieve full ZVS under light-load conditions and minimize the peak current under heavy-load conditions. Furthermore, the optimal magnetic component parameters are designed in combination with this optimal modulation strategy under variable load conditions. This approach can not only minimize the current stress, reducing both peak and rms currents, but also ensure full ZVS under light-load conditions.

Several conclusions can be drawn from experimental results: 1) the current stress with the designed inductance and turns ratio was consistently lower than that of the other magnetic component parameters; 2) full ZVS can be achieved under light-load conditions; 3) compared with other methods, the proposed method effectively reduces both peak current and rms current, leading to a significant improvement in efficiency under the given operating conditions.

REFERENCES

[1] R. W. A. A. De Doncker, D. M. Divan, and M. H. Kheraluwala, "A three-phase soft-switched high-power-density DC/DC converter for high-power applications," *IEEE Trans. Ind. Appl.*, vol. 27, no. 1, pp. 63–73, Jan./Feb. 1991.

[2] S. Inoue and H. Akagi, "A bidirectional isolated DC–DC converter as a core circuit of the next-generation medium-voltage power conversion system," *IEEE Trans. Power Electron.*, vol. 22, no. 2, pp. 535–542, Mar. 2007.

[3] B. Zhao, Q. Song, W. Liu, and Y. Sun, "Overview of dual-active-bridge isolated bidirectional DC–DC converter for high-frequency-link power-conversion system," *IEEE Trans. Power Electron.*, vol. 29, no. 8, pp. 4091–4106, Aug. 2014.

[4] Y. Lu, Q. Wu, Q. Wang, D. Liu, and L. Xiao, "Analysis of a novel zero-voltage-switching bidirectional DC/DC converter for energy storage system," *IEEE Trans. Power Electron.*, vol. 33, no. 4, pp. 3169–3179, Apr. 2018.

[5] N. M. L. Tan, T. Abe, and H. Akagi, "Design and performance of a bidirectional isolated DC–DC converter for a battery energy storage system," *IEEE Trans. Power Electron.*, vol. 27, no. 3, pp. 1237–1248, Mar. 2012.

[6] D. Sha, G. Xu, and Y. Xu, "Utility direct interfaced charger/discharger employing unified voltage balance control for cascaded H-bridge units and decentralized control for CF-DAB modules," *IEEE Trans. Ind. Electron.*, vol. 64, no. 10, pp. 7831–7841, Oct. 2017.

[7] F. Krismer and J. W. Kolar, "Accurate power loss model derivation of a high-current dual active bridge converter for an automotive application," *IEEE Trans. Ind. Electron.*, vol. 57, no. 3, pp. 881–891, Mar. 2010.

[8] H. Akagi, T. Yamagishi, N. M. L. Tan, S. Kinouchi, Y. Miyazaki, and M. Koyama, "Power-loss breakdown of a 750-V 100-kW 20-kHz bidirectional isolated DC–DC converter using SiC-MOSFET/SBD dual modules," *IEEE Trans. Ind. Appl.*, vol. 51, no. 1, pp. 420–428, Jan. 2015.

[9] R. Haneda and H. Akagi, "Power-loss characterization and reduction of the 750-V 100-KW 16-KHz dual-active-bridge converter with buck and boost mode," *IEEE Trans. Ind. Appl.*, vol. 58, no. 1, pp. 541–553, Jan. 2022.

[10] H. Fan and H. Li, "High-frequency transformer isolated bidirectional DC–DC converter modules with High efficiency over wide load range for 20 kVA solid-State transformer," *IEEE Trans. Power Electron.*, vol. 26, no. 12, pp. 3599–3608, Dec. 2011.

[11] H. Shi et al., "Minimum-backflow-power scheme of DAB-based solid-State transformer with extended-phase-shift control," *IEEE Trans. Ind. Appl.*, vol. 54, no. 4, pp. 3483–3496, Jul./Aug. 2018.

[12] A. Tong, L. Hang, G. Li, X. Jiang, and S. Gao, "Modeling and analysis of a dual-active-bridge-isolated bidirectional DC/DC converter to minimize RMS current with whole operating range," *IEEE Trans. Power Electron.*, vol. 33, no. 6, pp. 5302–5316, Jun. 2018.

[13] J. Li, Q. Luo, D. Mou, Y. Wei, P. Sun, and X. Du, "A hybrid five-variable modulation scheme for dual-active-bridge converter with minimal RMS current," *IEEE Trans. Ind. Electron.*, vol. 69, no. 1, pp. 336–346, Jan. 2022.

[14] S. Chakraborty and S. Chattopadhyay, "Fully ZVS, minimum RMS current operation of the dual-active half-bridge converter using closed-loop three-degree-of-freedom control," *IEEE Trans. Power Electron.*, vol. 33, no. 12, pp. 10188–10199, Dec. 2018.

[15] D. Mou et al., "Hybrid duty modulation for dual active bridge converter to minimize RMS current and extend soft-switching range using the frequency domain analysis," *IEEE Trans. Power Electron.*, vol. 36, no. 4, pp. 4738–4751, Apr. 2021.

[16] J. Huang, Y. Wang, Z. Li, and W. Lei, "Unified triple-phase-shift control to minimize current stress and achieve full soft-switching of isolated bidirectional DC–DC converter," *IEEE Trans. Ind. Electron.*, vol. 63, no. 7, pp. 4169–4179, Jul. 2016.

[17] Q. Gu, L. Yuan, J. Nie, J. Sun, and Z. Zhao, "Current stress minimization of dual-active-bridge DC–DC converter within the whole operating range," *IEEE J. Emerg. Sel. Topics Power Electron.*, vol. 7, no. 1, pp. 129–142, Mar. 2019.

[18] N. Hou, W. Song, and M. Wu, "Minimum-current-stress scheme of dual active bridge DC–DC converter with unified phase-shift control," *IEEE Trans. Power Electron.*, vol. 31, no. 12, pp. 8552–8561, Dec. 2016.

[19] N. Hou and Y. W. Li, "Overview and comparison of modulation and control strategies for a nonresonant single-phase dual-active-bridge DC–DC converter," *IEEE Trans. Power Electron.*, vol. 35, no. 3, pp. 3148–3172, Mar. 2020.

[20] L. Li, G. Xu, W. Xiong, D. Liu, and M. Su, "An optimized DPS control for dual-active-bridge converters to secure full-load-range ZVS with low current stress," *IEEE Trans. Transp. Electrific.*, vol. 8, no. 1, pp. 1389–1400, Mar. 2022.

[21] S. Chaurasiya and B. Singh, "A load adaptive hybrid DPS control for DAB to secure minimum current stress and full ZVS operation over wide load and voltage conversion ratio," *IEEE Trans. Ind. Appl.*, vol. 59, no. 2, pp. 1901–1911, Mar./Apr. 2023.

[22] B. Zhao, Q. Yu, and W. Sun, "Extended-phase-shift control of isolated bidirectional DC–DC converter for power distribution in microgrid," *IEEE Trans. Power Electron.*, vol. 27, no. 11, pp. 4667–4680, Nov. 2012.

[23] G. Xu, L. Li, X. Chen, Y. Liu, Y. Sun, and M. Su, "Optimized EPS control to achieve full load range ZVS with seamless transition for dual active bridge converters," *IEEE Trans. Ind. Electron.*, vol. 68, no. 9, pp. 8379–8390, Sep. 2021.

[24] Z. Guo and X. Han, "Control strategy of AC-DC converter based on dual active bridge with minimum current stress and soft switching," *IEEE Trans. Power Electron*, vol. 37, no. 9, pp. 10178–10189, Sep. 2022.

[25] H. Zhang, Z. Liu, Y. Song, P. Han, and J. Liu, "A current-stress-optimized design method for dual active bridge converters with improved ZVS capability under wide output voltage conditions," *IEEE Trans. Ind. Electron.*, vol. 71, no. 6, pp. 5807–5817, Jun. 2024.

[26] A. N, S. J. T.G., and V. John, "Minimum leakage inductance for soft switching of dual-active half-bridge DC-DC converter," in *Proc. IEEE Int. Conf. Power Electron., Drives Energy Syst.*, 2020, pp. 1–6.

[27] A. Jafari, M. S. Nikoo, F. Karakaya, and E. Matioli, "Enhanced DAB for efficiency preservation using adjustable-tap high-frequency transformer," *IEEE Trans. Power Electron.*, vol. 35, no. 7, pp. 6673–6677, Jul. 2020.

[28] X. Chen, G. Xu, H. Han, D. Liu, Y. Sun, and M. Su, "Light-load efficiency enhancement of high-frequency dual-active-bridge converter under SPS control," *IEEE Trans. Ind. Electron.*, vol. 68, no. 12, pp. 12941–12946, Dec. 2021.

[29] C. Gammeter, F. Krismer, and J. W. Kolar, "Comprehensive conceptualization, design, and experimental verification of a weight-optimized all-SiC 2 kV/700 V DAB for an airborne wind turbine," *IEEE J. Emerg. Sel. Topics Power Electron.*, vol. 4, no. 2, pp. 638–656, Jun. 2016.

[30] V. M. Iyer, S. Gulur, and S. Bhattacharya, "Optimal design methodology for dual active bridge converter under wide voltage variation," in *Proc. IEEE Transport. Electrific. Conf. Expo.*, 2017, pp. 413–420.

[31] D. Das and K. Basu, "Optimal design of a Dual-Active-bridge DC–DC converter," *IEEE Trans. Ind. Electron.*, vol. 68, no. 12, pp. 12034–12045, Dec. 2021.

[32] Y. Yan, H. Bai, A. Foote, and W. Wang, "Securing full-power-range zero-voltage switching in both steady-State and transient operations for a dual-active-bridge-based bidirectional electric vehicle charger," *IEEE Trans. Power Electron.*, vol. 35, no. 7, pp. 7506–7519, Jul. 2020.

[33] Z. Guo, "Modulation scheme of dual active bridge converter for seamless transitions in multiworking modes compromising ZVS and conduction loss," *IEEE Trans. Ind. Electron.*, vol. 67, no. 9, pp. 7399–7409, Sep. 2020.

[34] S. Dusmez, A. Hasanzadeh, and A. Khaligh, "Comparative analysis of bidirectional three-level DC–DC converter for automotive applications," *IEEE Trans. Ind. Electron.*, vol. 62, no. 5, pp. 3305–3315, May 2015.

[35] I. Villar, U. Viscarret, I. Etxeberria-Otadui, and A. Rufer, "Global loss evaluation methods for nonsinusoidally fed medium-frequency power transformers," *IEEE Trans. Ind. Electron.*, vol. 56, no. 10, pp. 4132–4140, Oct. 2009.

[36] O. J. Hector, "AC resistance evaluation of foil, round and Litz conductors in magnetic components," Ph.D. dissertation, Dept. Electr. Pow. Eng., Chalmers Univ. Technol., Gothenburg, Sweden, 2013.

Hongwei Zhang (Student Member, IEEE) received the B.S. degree in electrical engineering from Fuzhou University, Fuzhou, China, in 2018. He is currently working toward the Ph.D. degree in power electronics with Xi'an Jiaotong University, Xi'an, China.

His current research interests include optimized design and modeling control of isolated dc–dc converters.

Zeng Liu (Senior Member, IEEE) received the B.S. degree from Hunan University, Changsha, China, in 2006, and the M.S. and Ph.D. degrees from Xi'an Jiaotong University (XJTU), Xi'an, China, in 2009 and 2013, respectively, all in electrical engineering.

He was with XJTU as a Faculty Member in electrical engineering, where he is currently an Associate Professor. From 2015 to 2017, he was with the Center for Power Electronics Systems, Virginia Polytechnic Institute and State University, Blacksburg, VA, USA, as a Visiting Scholar. His research interests include control and stability of power electronics systems with multiple converters for renewable energy and energy storage applications.

Dr. Liu was the recipient of two Prize Paper Awards in IEEE TRANSACTIONS ON POWER ELECTRONICS, and the CPSS Science and Technology Progress Award. He is currently an Associate Editor for the IEEE OPEN JOURNAL OF POWER ELECTRONICS and on the Editorial Board for the ENERGIES, and served as Secretary-General for *2019 IEEE 10th International Symposium on Power Electronics for Distributed Generation Systems* and *2020 the 4th International Conference on HVDC*.